

RESEARCH ARTICLE

Feedforward combined multi-axis cross-coupling contour control compensation strategy of optical mirror processing robot

Zujin Jin¹, Gang Cheng^{1,2,*}  and Yutong Meng¹

¹School of Mechatronic Engineering, China University of Mining and Technology, Xuzhou 221116, China and ²Shangdong Zhongheng Optoelectronic Technology Co., Ltd., Zaozhuang 277000, China

*Corresponding author. E-mail: chg@cumt.edu.cn

Received: 6 May 2021; **Revised:** 27 January 2022; **Accepted:** 20 February 2022; **First published online:** 25 March 2022

Keywords: parallel manipulators, contour error, control compensation, contour control, multi-axis cross-coupling

Abstract

During the movement of an optical mirror processing robot (OMPR), the movement error of each branch chain leads to contour errors of the grinding tool, which reduce the accuracy of the optical mirror surface. To improve the processing accuracy of an OMPR, it is necessary to study the control and compensation strategy of its contour error. In this study, first, a kinematics analysis of an OMPR is conducted, and the trajectory of the end execution point in the world coordinate system is transformed into the fixed coordinate system of the robot. Combined with the common trajectory of optical mirror processing, based on the Frenet coordinate system, contour error models of the OMPR in straight line, arc, and spiral trajectories are established. Subsequently, the contour error, feedforward channel gain, and compensation channel gain models of the parallel module are established in the task space, and concurrently, the control variables and stability of the system are analyzed. Finally, the established feedforward combined multi-axis cross-coupling contour control compensation strategy is analyzed experimentally to verify its accuracy and effectiveness. It provides a theoretical basis for a robot to directly face the precision processing object using the control and compensation strategy in a future research study to improve the molding accuracy of a surface and optimize the processing technology of a large-scale optical mirror.

1. Introduction

Using evolving technology, modern optical mirrors are being developed with increased apertures and enhanced precision, which have high requirements in optical mirror processing robots (OMPRs) [1, 2]. In the optical mirror processing process, the grinding system of an OMPR is required to reach any position in the processing space with any posture. The four processing steps of the mirror surface—rough grinding, milling, fine grinding, and polishing—can be completed by the OMPR [3, 4]. Based on this, a five-degree-of-freedom (5-DOF) hybrid processing robot is designed [5–7]. In the OMPR process, the motion error of each motion branch and the rotation axis [8, 9] causes a contour error of the end execution point of the grinding system [10]. Moreover, if the theoretical trajectory deviates from the actual track, it will lead to an uncertainty of the dwell time, and the removal amount of the optical mirror will not meet the Gaussian distribution [11]. Therefore, it is necessary to analyze and study the end contour error of an OMPR and improve its machining accuracy by control compensation [12, 13].

Numerous research studies have been conducted on contour error modeling methods. To improve the estimation accuracy of contour errors, Liu et al. developed an iterative algorithm based on the osculating circle method to re-evaluate chord errors [14]. Izadbakhsh et al. proposed a new observer–controller structure based on function approximation techniques and Stone–Weierstrass theorem using differential equations and proved that the controller has good performance in overcoming uncertainty and reducing tracking error [15]. To reduce the contour error in contour-following tasks, Du et al. proposed a contour

error estimation method based on a third-order osculating helix [16]. Yang et al. focused on developing a nearest point projection curvature circle iterative algorithm to achieve real-time estimation of multi-axis contouring errors [17]. Song et al. proposed a third-order estimation algorithm for a defined joint-space contour error, using the concept of a generalized curve [18]. Ma et al. proposed a subregional toolpath regeneration method for contour-parallel processing based on the isoscallop method, which reduced the profile arithmetic average error and the maximum of profile deviation decrease [19]. Considering the geometric characteristics of corner-smoothed five-axis tool paths, Hu et al. proposed an online and high-accuracy contour error estimation algorithm for five-axis computer numerical control (CNC) machining [20]. To obtain an accurate analytical expression of free space contour errors, Wang et al. proposed a spatial contour error estimation method based on the double Taylor expansion [21]. Song et al. proposed a third-order contour error estimation algorithm to improve contour error estimation accuracy without iterative computation [22]. Sheng et al. proposed a comparison strategy to improve the accuracy of traditional contour error estimation [23]. A novel computationally efficient contouring error estimation method for contouring control was presented by Yang et al., which eliminates the abrupt changes in contouring error vector directions that are encountered by traditional contouring error estimation methods in large-curvature regions [24]. To simultaneously achieve accurate contouring error estimation and high-performance contouring control for three-dimensional contouring-following tasks, Hu et al. proposed a numerical calculation-based contouring error estimation and contour compensation scheme [25].

Machine tools have their own dynamic characteristics to improve the adaptability of the control compensation. Numerous scholars have also conducted research and application for the contour error control and compensation of different machine tools. To improve the accuracy of large-curvature position tracking and contour control, Zhang et al. proposed a position compensation method composed of a cross-coupling controller and an improved position error compensator [26]. Izadbakhsh et al. designed the controller of electric manipulator with Szász–Mirakyan operator as the basis function and proved that Szász–Mirakyan operator plays a good role in uncertainty compensation and improving tracking error [27]. To improve the contour error control accuracy of a networked multi-axis motion system with a time-varying time delay, Wang et al. designed a linear active disturbance rejection controller for uniaxial trajectory tracking control [28]. Li et al. presented the method of online self-tuning proportional–derivative controller to improve the control performance of robot contour control [29]. For five-axis machine tools, Chen et al. proposed a new contour error precompensation method that integrates the analytical prediction of the contour error, an optimal path-reshaping model, and a decoupling solution algorithm [30]. Aiming at high-precision control of CNC machine tools, Li et al. presented a contour error estimation algorithm for digital curves based on a geometrical method [31]. To solve the problems of time delay and time lag of contour error compensation by a feedback control, Wang et al. proposed a new position loop feedforward contour control method [32]. Duong et al. presented an offline gain adjustment approach to reduce the contour error in five-axis high-speed machining [33]. Cho et al. presented a novel neural network-based proportional–integral–derivative (PID) controller gain update algorithm. The proposed algorithm aimed to improve machining quality and efficiency by adjusting the PID gains in real time to minimize the contour error [34]. In order to improve the trajectory tracking precision of a six-DOF lightweight robot, Liu et al. proposed a nonlinear proportion-deviation cross-coupling synchronization control strategy based on adjacent coupling error analysis [35]. Wang et al. proposed a Newton extremum-seeking algorithm-based iterative learning coordinated control strategy for contouring motion accuracy of precision multi-axial systems [36]. By considering the coupling effects among multiple axes, Ouyang et al. proposed a cross-coupled PID control developed in the position domain and subsequently applied the controller to a multi-axis CNC machine for contour tracking performance improvement [37].

Although there have been considerable research and application efforts on contour error modeling and contour control compensation using different methods, the contour error models are established under different working conditions, the contour error compensation control strategies are formulated under related tasks, and certain results are achieved. Moreover, most studies have focused on multi-axis CNC machine tools, and there is no in-depth study on a 5-DOF hybrid robot, which has complex

dynamic characteristics. In addition, there is no relevant literature to analyze the contour error of the dwell point combined with the polishing process characteristics of the optical mirror.

In this study, the contour error and control compensation strategy of a five-DOF OMPR are studied and analyzed. The Frenet coordinate system is established based on the principle of differential geometry. Using the tangential approximation and osculating circle approximation methods, three-dimensional contour error models of the machining robot in grid trajectory, concentric circle trajectory, and spiral trajectory processing modes are derived. The control strategy of the entire machine is determined, and a parallel module feedforward combined cross-coupling control system is built. Based on the kinematic transformation relationship, the contour error control, feedforward channel gain, and compensation channel gain models are established in the parallel module task space. Subsequently, the transfer function of the cross-coupling system is deduced, and the key control variables and stability of the system are analyzed. Finally, using an experimental prototype, a contour error control compensation experiment analysis is conducted on the tool path commonly used in optical mirror processing, and the contour control strategy and related theories are verified.

2. OMPR

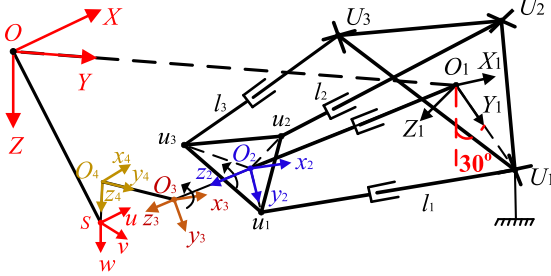
Based on the grinding process requirements, the OMPR requires at least five DOFs. The robot used in this study was a five-DOF OMPR developed using a three-DOF parallel (3UPS + UP: U - hook joint, P - moving pair, S - ball joint) manipulator combined with a two-DOF serial manipulator. The five-DOF OMPR consisted of a fixed platform, drive branch chain, constrained branch chain, moving platform, and two-DOF serial manipulator. The topological structure and prototype of the OMPR are shown in Fig. 1(a) and (b); there are three UPS drive branches and one UP constraint branch link between the movable and fixed platforms. The world coordinate system, $O-XYZ$, is established at the center point, O , of the mirror to be processed, the Z axis is downward, the Y axis points to the center point of the robot fixed platform, and the X axis is determined based on the right-hand rule. The fixed platform is installed at an angle of 30° with the Z axis of the world coordinate system. A fixed coordinate system, $O_1-X_1Y_1Z_1$, is established on the center, O_1 , of the fixed platform, the Y_1 axis is along the $\overline{O_1U_1}$ direction, the Z_1 axis is perpendicular to the fixed platform, and the X_1 axis is determined by the right-hand rule. A moving coordinate system, $O_2-x_2y_2z_2$, is established on the central point, O_2 , of the moving platform, the y_2 axis is along the $\overline{O_2u_1}$ direction, and the z_2 axis is perpendicular to the moving platform. Moreover, the x_2 axis is determined by the right-hand rule. The coordinate system, $O_3-x_3y_3z_3$, is established on the junction point, O_3 , of the two series rotating heads. The x_3 axis is collinear with the axis of the secondary rotating head, and the y_3 axis is determined by the right-hand rule. The secondary rotating head coordinate system, $O_4-x_4y_4z_4$, is set up on tool spindle O_4 point, the z_4 axis is down the tool spindle, the y_4 axis is along the direction, and the x_4 axis is determined by the right-hand rule. The tool coordinate system, $S-uvw$, is established on the end tool execution point, S , and the w axis is the normal direction of the mirror to be processed. The u axis is the tangent direction of the tool path, and the v axis is determined based on the right-hand rule. The end grinding tool uses computer controlled optical surfacing (CCOS) grinding system, and its structure is shown in Fig. 1(c). The CCOS grinding system consists of a rotating motor and a revolving motor, which uses a smaller grinding head for grinding.

When the OMPR performs a processing task, a transformation relationship needs to be established to convert the end execution point in the world coordinate system to the fixed coordinate system.

$${}^oP = q_1 + {}^oR_{O_1} {}^{O_1}P, \tag{1}$$

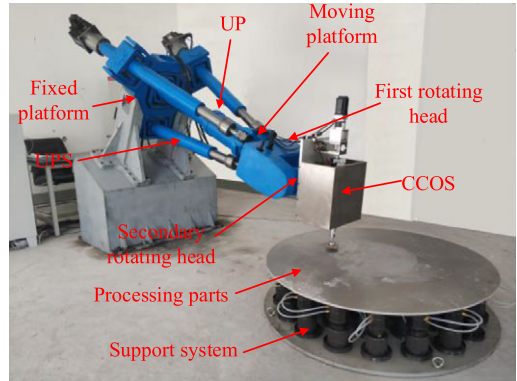
where oP is the position vector of any point in the world coordinate system, q_1 is the position vector of the center point of the fixed platform under $O-XYZ$, ${}^{O_1}P$ is the position vector of point P under $O_1-X_1Y_1Z_1$, and ${}^oR_{O_1}$ is the transformation matrix from $O-XYZ$ to $O_1-X_1Y_1Z_1$.

(a)



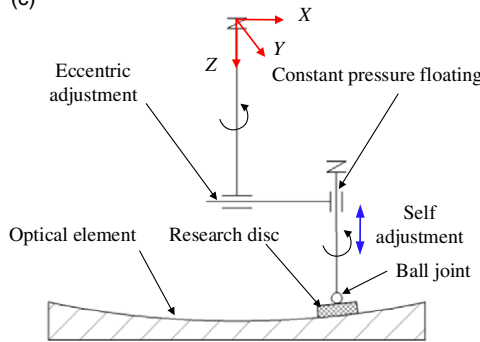
Topology of the OMPR

(b)



Prototype of the OMPR

(c)



Topology of CCOS grinding system

Figure 1. OMPR.

(1) Inverse solution of series module

In the world coordinate system, the end point of the grinding tool on the curved surface is $S = [x_0 \ y_0 \ z_0]^T$, and a smooth trajectory curve through the point S is given as follows:

$$\Gamma: \begin{cases} x = x(t) \\ y = y(t) \\ z = z(t). \end{cases} \tag{2}$$

Subsequently, the tangent vector, u , of Γ at point S and the normal vector, w , of the surface are

$$\begin{cases} u = \frac{[\dot{x}_0(t_0) \ \dot{y}_0(t_0) \ \dot{z}_0(t_0)]^T}{\sqrt{\dot{x}_0(t_0)^2 + \dot{y}_0(t_0)^2 + \dot{z}_0(t_0)^2}} \\ w = \frac{[\ell_x(x_0 \ y_0 \ z_0) \ \ell_y(x_0 \ y_0 \ z_0) \ \ell_z(x_0 \ y_0 \ z_0)]^T}{\sqrt{\ell_x(x_0 \ y_0 \ z_0)^2 + \ell_y(x_0 \ y_0 \ z_0)^2 + \ell_z(x_0 \ y_0 \ z_0)^2}}, \end{cases} \tag{3}$$

where ℓ_x is the partial derivative of the surface equation to x , and t_0 is the value at a certain time.

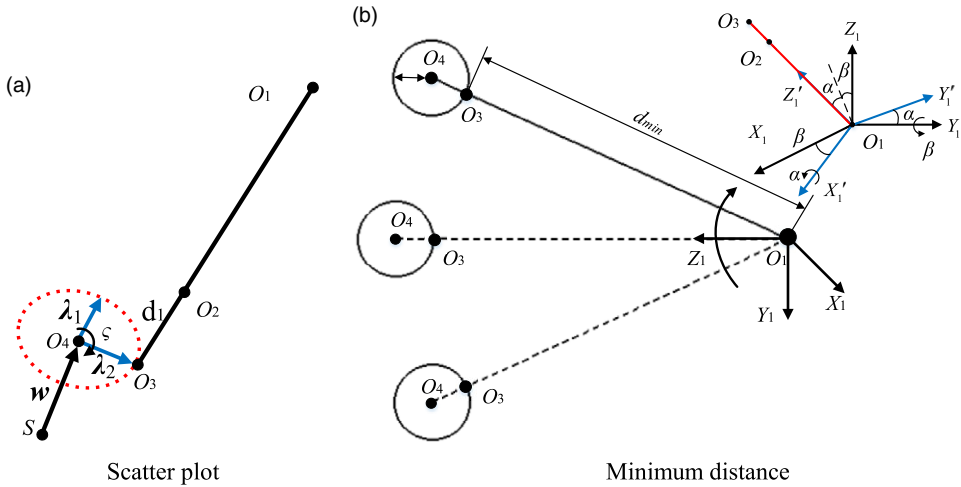


Figure 2. Schematic of numerical search method.

Subsequently, the posture matrix of the end grinding tool coordinate system in the O - XYZ coordinate system is obtained as

$$R_d = [u \quad v \quad w]_{3 \times 3} \tag{4}$$

where $v = u \times w$.

Thus, the vector of point O_4 in the O - XYZ coordinate system is

$${}^oO_4 = S - R_d \cdot q_2 \tag{5}$$

where q_2 is the position vector of point S in the O_4 - $x_4y_4z_4$.

In Figure 2(a), the relative position vector of O_3 and O_2 is typically unchanged in the moving platform coordinate system, O_2 - $x_2y_2z_2$. Therefore,

$$r_2 = r_3 - d_1n, \tag{6}$$

where r_2 is the position vector of O_2 under O_1 - $X_1Y_1Z_1$, r_3 is the position vector of O_3 under O_1 - $X_1Y_1Z_1$, n is the direction vector of $\overline{O_3O_1}$, and d_1 is the distance between O_2 and O_3 .

Based on the structure of the two tandem rotating heads and cutter tools, the O_3 point is continuously distributed on the plane circle with the O_4 point as the center and d_2 as the radius. According to the characteristics of the vector cross-product, two vertical vectors in the plane circle are found,

$$\begin{cases} \lambda_1 = \frac{{}^oO_4 \times E^1}{|{}^oO_4 \times E^1|} \\ \lambda_2 = \frac{\lambda_1 \times {}^oO_4}{|\lambda_1 \times {}^oO_4|} \end{cases} \tag{7}$$

where E^1 is a unit vector, λ_1 is the unit direction vector perpendicular to oO_4 , and λ_2 is the unit direction vector perpendicular to λ_1 and oO_4 .

Using the numerical search method, on the circle having O_4 as the center, w as the central axis, and d_2 as the radius, vectors λ_1 and λ_2 are searched clockwise in a certain step ζ from 0 to 2π , and a series of scattered points are obtained. The positions of the scattered points in the world coordinate system can

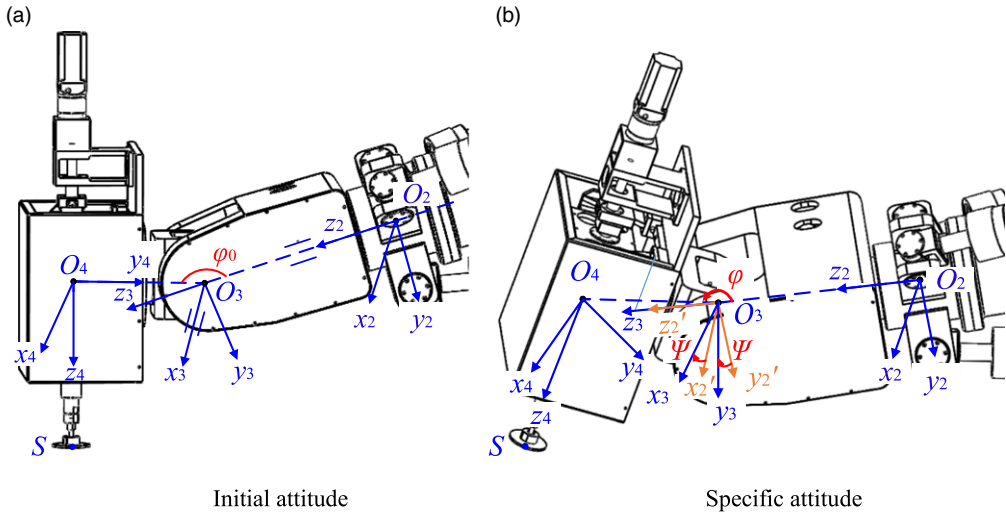


Figure 3. Attitude diagram of series module.

be expressed as

$$\begin{cases} x_s = {}^oO_{4x} + d_2\lambda_{1x} \cos(\zeta) + d_2\lambda_{2x} \sin(\zeta) \\ y_s = {}^oO_{4y} + d_2\lambda_{1y} \cos(\zeta) + d_2\lambda_{2y} \sin(\zeta) \\ z_s = {}^oO_{4z} + d_2\lambda_{1z} \cos(\zeta) + d_2\lambda_{2z} \sin(\zeta), \end{cases} \tag{8}$$

where ${}^oO_{4x}$, ${}^oO_{4y}$, and ${}^oO_{4z}$ are the components of oO_4 along the coordinate axis of the world coordinate system; λ_{1x} , λ_{1y} , and λ_{1z} are the components of λ_1 along each coordinate axis of the world coordinate system; and λ_{2x} , λ_{2y} , and λ_{2z} are the components of λ_2 along each coordinate axis of the world coordinate system.

As shown in Fig. 2(b), the motion of point O_3 in the parallel module essentially adopts the fixed platform center point, O_1 , as the fulcrum to swing around the X_1 and Y_1 axes. Therefore, the minimum distance to the O_1 point can be used to constrain the scattered points, and the position vector of the O_3 point in the world coordinate system $O-XYZ$ can be obtained.

During the machining process, angles ψ and φ of the two tandem rotating heads are fine-tuned. Figure 3 shows the posture of the OMPR.

At present, the positions of points S , O_4 , O_3 , and O_1 in the world coordinate system are known, and the rotation angle of the first rotating head and secondary rotating head is obtained as

$$\varphi = \arccos \left(\frac{\overline{O_3O_4} \cdot \overline{O_3O_1}}{\left| \overline{O_3O_4} \right| \left| \overline{O_3O_1} \right|} \right). \tag{9}$$

$$\psi = \arccos(\mathbf{x}_3 \cdot \mathbf{x}_2') \tag{10}$$

where \mathbf{x}_3 and \mathbf{x}_2' are the unit vector expressions of the x_3 and x_2' axes.

(2) Kinematics of parallel module

Based on Fig. 1, O_1 , O_2 , U_i , and u_i can form closed-loop vectors ($i = 1, 2, 3$); therefore,

$$\begin{cases} \mathbf{r}_{U_i} + l_i \mathbf{e}_i = \mathbf{r}_{u_i} + \mathbf{r}_2 \\ \mathbf{r}_2 = L_2 \mathbf{e}_L, \end{cases} \tag{11}$$

where L_2 is the length of the UP branch chain with O_2 as the end, l_i and e_i are the length and unit direction vector of branch chain i , $e_L = n$ is the unit direction vector of the UP branch chain under $O_1-X_1Y_1Z_1$, r_2 is the position vector of point O_2 under $O_1-X_1Y_1Z_1$, r_{ui} is the position vector of U_i in $O_1-X_1Y_1Z_1$, and r_{ui} is the position vector of u_i in $O_1-X_1Y_1Z_1$.

The lengths of the UPS and UP chains change as follows:

$$l_i = \sqrt{(r_2 + r_{ui} - r_{Ui})^T (r_2 + r_{ui} - r_{Ui})} \tag{12}$$

and

$$L_2 = e_L^T r_2. \tag{13}$$

Furthermore, the velocity of the UP constrained branch chain and the angular velocity of the moving platform are obtained as follows:

$$\dot{L}_2 = e_L^T \dot{r}_2 \quad \text{and} \tag{14}$$

$$\omega = \frac{e_L \times \dot{r}_2}{L_2} = \frac{e_{L \times}}{L_2} \dot{r}_2, \tag{15}$$

where $e_{L \times} = \begin{bmatrix} 0 & -e_{Lz} & e_{Ly} \\ e_{Lz} & 0 & -e_{Lx} \\ -e_{Ly} & e_{Lx} & 0 \end{bmatrix}$ is the third-order antisymmetric matrix of e_L and \dot{r}_2 is the speed of the moving platform.

The expansion acceleration of the UP branch chain and the angular acceleration of the moving platform are

$$\ddot{L}_2 = e_L^T \ddot{r}_2 + (\omega \times e_L)^T \dot{r}_2 = J_L \ddot{r}_2 + \dot{J}_L \dot{r}_2, \tag{16}$$

$$\dot{\omega} = \frac{e_{L \times}}{L_2} \ddot{r}_2 + \left[\frac{(e_L \times \omega)_\times}{L_2} - \frac{\dot{L}_2}{L_2^2} e_{L \times} \right] \dot{r}_2 = J_{d\omega} \ddot{r}_2 + \dot{J}_{d\omega} \dot{r}_2. \tag{17}$$

The speed and acceleration of the UPS branch chain are

$$\begin{cases} \dot{L} = J \dot{r}_2 \\ \ddot{L} = J \ddot{r}_2 + \dot{J} \dot{r}_2 \end{cases}, \tag{18}$$

where $J = \left[e_1 - \frac{e_1^T e_{Lr_{u1}}}{L_2} \quad e_2 - \frac{e_2^T e_{Lr_{u2}}}{L_2} \quad e_3 - \frac{e_3^T e_{Lr_{u3}}}{L_2} \right]_{3 \times 3}^T$,

$$\begin{aligned} \dot{J} &= \left[\omega_1 \times e_1 \quad \omega_2 \times e_2 \quad \omega_3 \times e_3 \right]^T + \frac{\dot{L}_2}{L_2^2} \left[e_1^T e_{Lr_{u1}} \quad e_2^T e_{Lr_{u2}} \quad e_3^T e_{Lr_{u3}} \right]^T \\ &\quad - \frac{1}{L_2} \begin{bmatrix} (\omega_1 \times e_1)^T e_{Lr_{u1}}^T + e_1^T (\omega_d \times e_L) r_{u1}^T + e_1^T e_L (\omega_d \times r_{u1})^T \\ (\omega_2 \times e_2)^T e_{Lr_{u2}}^T + e_2^T (\omega_d \times e_L) r_{u2}^T + e_2^T e_L (\omega_d \times r_{u2})^T \\ (\omega_3 \times e_3)^T e_{Lr_{u3}}^T + e_3^T (\omega_d \times e_L) r_{u3}^T + e_3^T e_L (\omega_d \times r_{u3})^T \end{bmatrix}, \end{aligned}$$

$$\dot{L} = [\dot{l}_1 \quad \dot{l}_2 \quad \dot{l}_3]^T, \quad \ddot{L} = [\ddot{l}_1 \quad \ddot{l}_2 \quad \ddot{l}_3]^T.$$

The angular velocity and angular acceleration of the UPS branch chain are

$$\omega_i = \frac{1}{l_i} \left[e_{i \times} + (e_i^T r_{ui} E - r_{ui} e_i^T) \frac{e_{L \times}}{L_2} \right] \dot{r}_2 = J_{\omega i} \dot{r}_2, \tag{19}$$

$$\dot{\omega}_i = J_{\omega i} \ddot{r}_2 + \dot{J}_{\omega i} \dot{r}_2, \tag{20}$$

where $\dot{J}_{\omega i} = -\frac{\dot{l}_i}{l_i^2} \left[e_{i \times} + (e_i^T r_{ui} E - r_{ui} e_i^T) J_{d\omega} \right] + \frac{1}{l_i} (\omega_i \times e_i)_\times + (e_i^T r_{ui} E - r_{ui} e_i^T) \dot{J}_{d\omega}$ and E is the third-order unit matrix.

The center of mass velocity of the UPS and UP branch chains is

$$v_{ci} = e_i J_i \dot{r}_2 - (l_i - l_{bi}) e_{i \times} J_{oi} \dot{r}_2, \tag{21}$$

$$v_{Ly} = e_L e_L^T \dot{r}_2 - (L_2 - L_y) \frac{1}{L_2} (E - e_L e_L^T) \dot{r}_2. \tag{22}$$

The accelerations of the center of masses of the UPS and UP branch chains are

$$\dot{v}_{ci} = \{ (\omega_i \times e_i) J_i + e_i \dot{J}_i + \dot{l}_i e_{i \times} J_{oi} - (l_i - l_{bi}) [(\omega_i \times e_i)_{\times} J_{oi} - (l_i - l_{bi}) e_{i \times} \dot{J}_{oi}] \} \dot{r}_2 + [e_i J_i - (l_i - l_{bi}) e_{i \times} J_{oi}] \ddot{r}_2, \tag{23}$$

$$\dot{v}_{Ly} = \left[(\omega_d \times e_L) J_y + e_L \dot{J}_y - (L_2 - L_y) \frac{1}{L_2} (\omega_d \times e_L) (\omega_d \times e_L)^T + \frac{L_y \dot{L}_2}{L_2^2} (E - e_L e_L^T) \right] \dot{r}_2 + \left[e_L e_L^T - (L_2 - L_y) \frac{1}{L_2} (E - e_L e_L^T) \right] \ddot{r}_2, \tag{24}$$

where L_y is the distance from the center of mass of driving chain 2 to O_2 , and J_y is the component of J in the y-direction.

Then, the dynamic model of the OMPR can be expressed as:

$$\tau = M_q \cdot \ddot{L} + C_q \cdot \dot{L} + G_q \tag{25}$$

where τ is the control input torque, M_q is the inertia matrix, $M_q = (J^{-1})^T M J^{-1}$, C_q is Coriolis force, $C_q = (J^{-1})^T M \dot{J}^{-1} + (J^{-1})^T C J^{-1}$, and G_q is gravity, $G_q = (J^{-1})^T G$. Due to the coupling force in the motion process of the parallel manipulator, the diagonal parts of M_q and C_q represent the force on the current joint, namely inertial force, Coriolis force, and centrifugal force, while the nondiagonal part is the force generated by one joint on other joints, that is, the coupling force. The following relationship can be obtained:

$$\begin{cases} M_{qf} = M_{qc} \cdot \ddot{L} \\ C_{qf} = C_{qc} \cdot \dot{L} \\ F_o = M_{qo} \cdot \ddot{L} + C_{qo} \cdot \dot{L} \end{cases} \tag{26}$$

where M_{qf} , C_{qf} , F_o are inertia force, Coriolis force and coupling force, respectively. And,

$$M_{qc} = \begin{bmatrix} M_q(1,1) & & \\ & M_q(2,2) & \\ & & M_q(3,3) \end{bmatrix}, M_{qo} = \begin{bmatrix} M_q(1,2) & M_q(1,3) \\ M_q(2,1) & M_q(2,3) \\ M_q(3,1) & M_q(3,2) \end{bmatrix},$$

$$C_{qc} = \begin{bmatrix} C_q(1,1) & & \\ & C_q(2,2) & \\ & & C_q(3,3) \end{bmatrix}, C_{qo} = \begin{bmatrix} C_q(1,2) & C_q(1,3) \\ C_q(2,1) & C_q(2,3) \\ C_q(3,1) & C_q(3,2) \end{bmatrix}.$$

Then, the dynamic model can be further expressed as:

$$\tau = M_{qf} \cdot \ddot{L} + C_{qf} \cdot \dot{L} + G_q + F_o \tag{27}$$

Since the active branch chain of the OMPR belongs to the single input single output model, it can be expressed as a linear constant continuous system:

$$\begin{cases} \dot{x}(t) = Ax(t) + Bu \\ y = Cx(t) \end{cases} \tag{28}$$

where $x(t) \in R^n$, $u \in R^m$, $A \in R^{n \times n}$ is a nonsingular matrix, $B \in R^{n \times m}$, $C \in R^{r \times n}$.

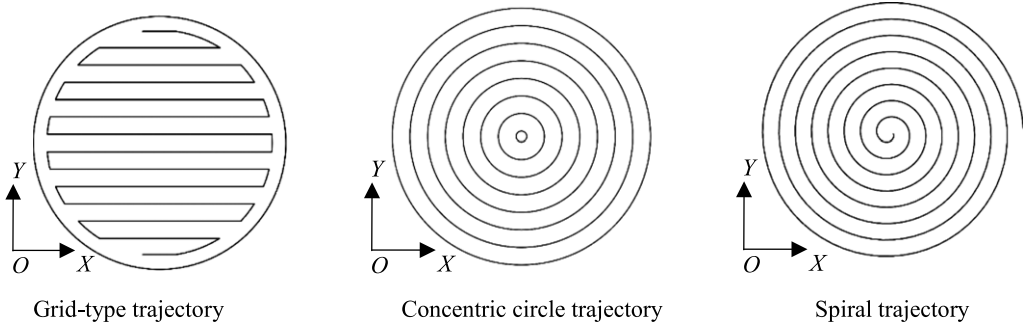


Figure 4. Tool paths.

3. Contour error analysis

In the process of optical mirror surface processing, the grinding tool accurately traverses each removal point on the mirror surface to be processed at a certain speed. As shown in Fig. 4, the commonly used tool paths at present are the grid, concentric circle, and spiral types.

For the OMPR to meet the processing requirements of different types of optical mirrors, the robot must be driven by the control system ensuring that the grinding tool can complete the above three types of contour movements.

The motion trajectory of the end grinding tool of the OMPR is composed of a series of interpolation points. The positions of these points can be described as vectors along the x , y , and z directions in the reference coordinate system, O -XYZ.

$$s(t) = [s_x(t) \quad s_y(t) \quad s_z(t)]^T, \quad t \in R, \tag{29}$$

where $s(t)$ represents the trajectory parameter of the grinding tool, which is a second-order derivable continuous smooth ideal contour.

Subsequently, the unit tangent vector of the motion trajectory can be expressed as

$$t(t) = \frac{\dot{s}(t)}{|\dot{s}(t)|}, \tag{30}$$

where $\dot{s}(t)$ is the velocity vector.

Thus, the principal normal vector at any point of the ideal trajectory of the grinding tool is defined as follows:

$$n(t) = \frac{\rho \cdot \dot{i}(t)}{|\rho \cdot \dot{i}(t)|}, \tag{31}$$

where ρ is the radius of curvature.

The tangent vector and the principal normal vector define a two-dimensional plane, which is called the osculating plane. In the three-dimensional space, there is a secondary normal vector at each point on the trajectory curve, which is perpendicular to the tangent vector and the principal normal vector. It is the second normal vector of the trajectory curve and is expressed as

$$b(t) = t(t) \times n(t). \tag{32}$$

$t(t)$, $n(t)$, and $b(t)$ form the Frenet coordinate system in the ideal position. As shown in Figure 5, D and A are the vectors of points D and A in O -XYZ, respectively, and the tracking error of the two points in O -XYZ is E_d . A_F is the position vector of point A in the Frenet coordinate system. Thus, the transformation relationship between the reference coordinate system, O -XYZ, and the Frenet coordinate system of point A is expressed as follows:

$$\begin{aligned} T_F: A &= R_F A_F + D \\ T_W: A_F &= R_F^{-1} E_d \end{aligned} \tag{33}$$

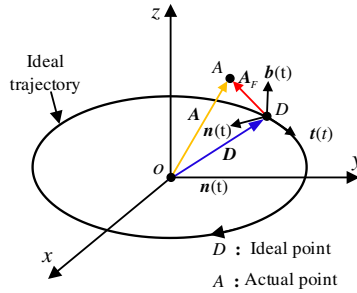


Figure 5. Frenet coordinate system transformation.

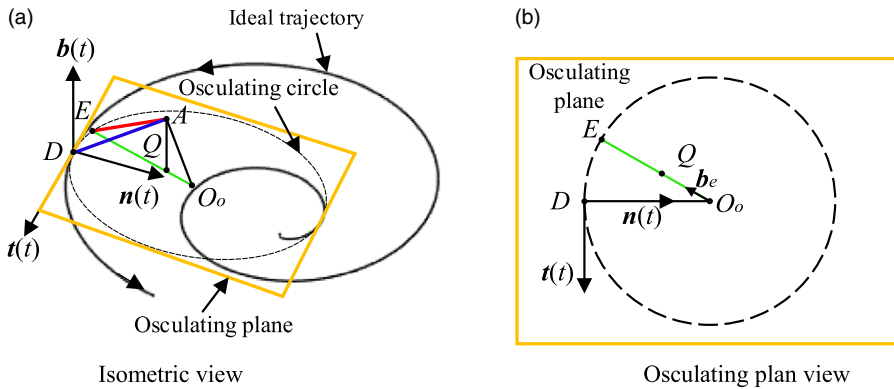


Figure 6. Three-dimensional contour error based on osculating circle.

where $R_F = [t \ n \ b]_{3 \times 3}$ is the coordinate transformation matrix, and $R_F^{-1} = R_F^T$. T_F represents the transformation from the Frenet coordinate system to the reference coordinate system, and T_W represents the transformation from the reference coordinate system to the Frenet coordinate system.

In the three-dimensional space, based on the Frenet coordinate system, the curvature and radius of curvature at a certain point can be obtained from the ideal trajectory of the grinding tool, and an osculating circle can be drawn. The contour error is solved using the shortest distance from the actual movement point of the grinding tool to the osculating circle.

The contour error of the spiral trajectory of the grinding tool in the three-dimensional space is shown in Fig. 6(a). Point Q is the projection point of point A on the osculating plane. Point E , which is closest to point A on the osculating circle, can be obtained. Thus, the contour error vector, ϵ , can be expressed as

$$\epsilon = [\overline{O_o A} \cdot b(t)] \cdot b(t) + [\rho - (\overline{O_o A} \cdot b_e)] \cdot b_e, \tag{34}$$

where $b_e = \frac{\overline{O_o Q}}{\|\overline{O_o Q}\|}$, and it is the unit orthogonal vector of b in the osculating plane.

The front view of a point projected onto the osculating plane is shown in Fig. 6(b), and the osculating circle is located in the osculating plane of the Frenet coordinate system. Among them, points E , Q , and O_o are on the same straight line. The contour error based on the osculating circle can be obtained as

$$\epsilon = \begin{bmatrix} 0 \\ 0 \\ -E_b \end{bmatrix} + \left(\frac{\rho}{\sqrt{E_t^2 + (E_n - \rho)^2}} - 1 \right) \cdot \begin{bmatrix} E_t \\ E_n - \rho \\ 0 \end{bmatrix}. \tag{35}$$

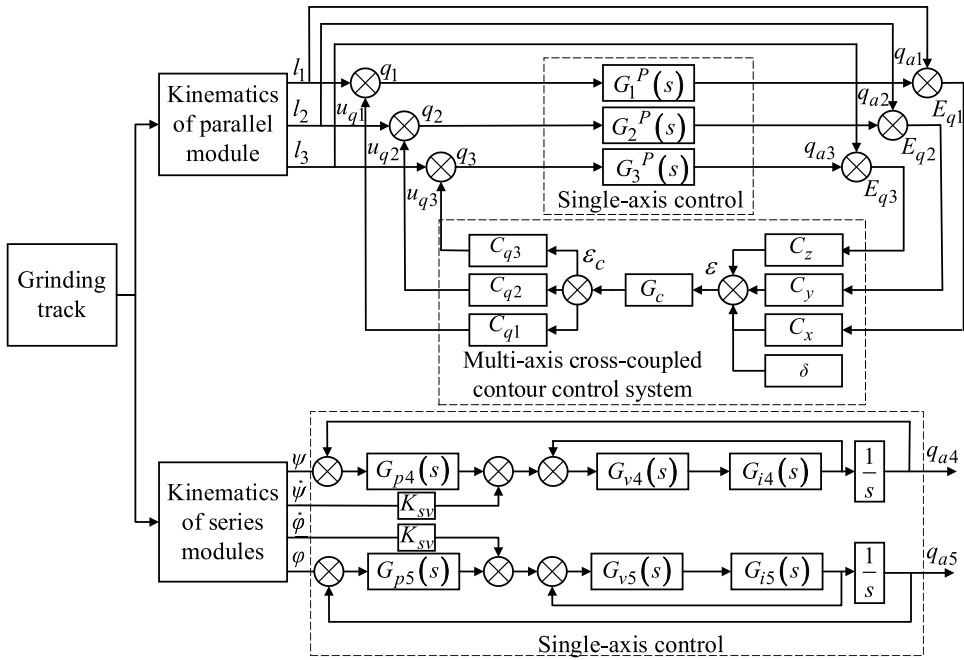


Figure 7. Contour control strategy of OMPR.

where E_l , E_n , and E_b are the components of the actual point of the end track along each axis of the Frenet coordinate system.

4. Feedforward combined multi-axis cross-coupling contour control

Compared to the parallel module, the series module has a lower speed, smaller range of motion, and smaller error. The series module can achieve higher motion accuracy by adopting a three-loop feedback control and speed feedforward. In this study, a cross-coupling control system is used to compensate the contour error at the end of the parallel module. Moreover, the parallel module single-joint servo control comprises speed and dynamic feedforward. The contour control strategy of the OMPR is shown in Fig. 7. Transfer functions $G_1^P(s)$, $G_2^P(s)$, $G_3^P(s)$, $G_4^P(s)$, and $G_5^P(s)$ are used to replace the relationship between the input and the output. q_{a1} , q_{a2} , q_{a3} , q_{a4} , and q_{a5} are the actual output joint displacements of the control system. Tracking errors E_{q1} , E_{q2} , and E_{q3} of the parallel module single-branch chain control system are input into the contour error model, and the contour error, ϵ , in the task space is calculated. The contour error control quantity, ϵ_c , is obtained using the cross-coupling controller, and a mathematical model of the compensation channel is established. The control variable, ϵ_c , is converted into the joint space and assigned to position loop input terminals u_{q1} , u_{q2} , and u_{q3} of the three drive branch chain servo control systems to obtain actual kinematic servo system input values q_1 , q_2 , and q_3 after compensation. C_x , C_y , and C_z are the forward channel gain coefficients; C_{q1} , C_{q2} , and C_{q3} are the compensation channel gain coefficients, and G_c is the cross-coupling controller. $G_{v4}(s)$ and $G_{v5}(s)$ are the transfer functions of the speed loop, $G_{i4}(s)$ and $G_{i5}(s)$ are the transfer functions of the current loop, and K_{sv} is the feedforward function of the speed loop.

The closed-loop control of UPS branch chain includes position loop, speed loop, current loop, and servo motor. And the structure of single-branch chain servo control system is shown in Fig. 8.

In the figure, K_p is the proportional coefficient of the position loop, K_{pv} is the proportional coefficient of the speed loop, τ_v is the time constant of the velocity loop, K_{pi} is the proportional coefficient of the current loop, τ_i is the current loop time constant, K_w is the proportional coefficient of PWM inverter,

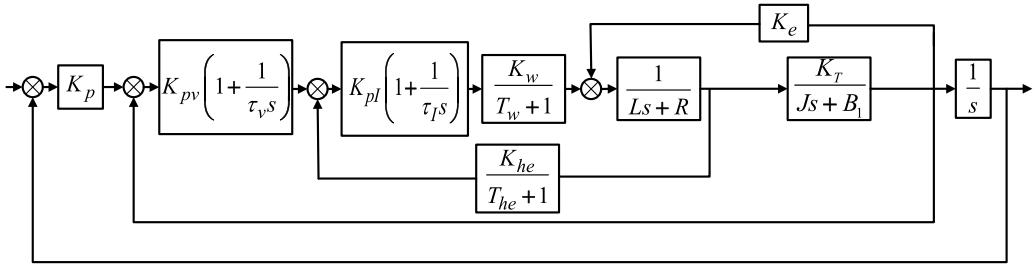


Figure 8. Servo control system of the UPS branch chain.

T_w is the switching frequency of PWM inverter, $T_h = 0.3 \sim 0.5T_w$, $K_h = 1$, R is the armature resistance, L is the armature inductance, K_T is the torque coefficient, K_e is the back EMF coefficient, J is the load moment of inertia of the motor, and B_1 is the viscous resistance.

To simplify the calculation, make: $K_{pv}(1 + \frac{1}{\tau_v s}) = G_1$, $K_{pl}(1 + \frac{1}{\tau_l s}) = G_2$, $\frac{K_w}{T_w + 1} = G_3$, $\frac{1}{Ls + R} = G_4$, $\frac{K_T}{Js + B_1} = G_5$, $\frac{K_{he}}{T_{he} + 1} = G_6$. Then, the transfer function of UPS branch chain is

$$G_i^P(s) = \frac{G_1 G_2 G_3 G_4 G_5 K_p}{(1 - G_2 G_3 G_4 G_6) (1 - G_4 G_5 K_e) s - G_1 G_2 G_3 G_4 G_5 s - G_1 G_2 G_3 G_4 G_5 K_p} \quad i = 1, 2, 3 \quad (36)$$

(1) Forward channel cross-coupling gain

To establish the transfer function for system analysis, the inverse of the error Jacobian matrix, J_e^{-1} , is used to map the tracking error of the parallel module from the joint space to the task space, and the tracking error of the end moving platform of the parallel module is obtained as follows:

$$E_d = \left[(e_1 \quad e_2 \quad e_3)^T - \frac{1}{L_2} (r_{u1} e_1^T e_L \quad r_{u2} e_2^T e_L \quad r_{u3} e_3^T e_L)^T \right]_{3 \times 3}^{-1} \cdot \begin{bmatrix} E_{q1} \\ E_{q2} \\ E_{q3} \end{bmatrix}_{3 \times 1} \quad (37)$$

The tracking errors in any direction of X_1 , Y_1 , and Z_1 at the end of the parallel module are caused by the coupling of the tracking errors of the three UPS branches. So the end tracking error, ${}^F E_d$, of the parallel module in the Frenet coordinate system can be calculated using the single-axis tracking error of the driving branch chain as follows:

$${}^F E_d = [t \quad n \quad b]_{3 \times 3}^{-1} \cdot J_e^{-1} \cdot E_q \quad (38)$$

The contour error in the task space of the parallel module can be calculated utilizing ${}^F E_d$ based on the osculating circle approximation methods.

$$e = K \cdot {}^F E_d + \delta, \quad (39)$$

where K is the contour error transfer matrix, $K = \begin{bmatrix} H & 0 & 0 \\ 0 & H & 0 \\ 0 & 0 & -1 \end{bmatrix}$, $\delta = \begin{bmatrix} 0 \\ -H \cdot \rho \\ 0 \end{bmatrix}$, and

$$H = \frac{\rho}{\sqrt{[(J_e^{-1} \cdot E_q)^T t]^2 + [(J_e^{-1} \cdot E_q)^T n - \rho]^2}} - 1.$$

Combining Fig. 7 and Eqs. (37) and (38), the forward channel gain of the cross-coupling control system is as follows:

$$\begin{cases} C_x = K \cdot \begin{bmatrix} t & n & b \end{bmatrix}_{3 \times 3}^{-1} \cdot J_e^{-1}(:, 1) \\ C_y = K \cdot \begin{bmatrix} t & n & b \end{bmatrix}_{3 \times 3}^{-1} \cdot J_e^{-1}(:, 2) \\ C_z = K \cdot \begin{bmatrix} t & n & b \end{bmatrix}_{3 \times 3}^{-1} \cdot J_e^{-1}(:, 3) \end{cases}, \tag{40}$$

The forward channel gain, ϵ , is obtained as follows:

$$\epsilon = C_x \cdot E_{q1} + C_y \cdot E_{q2} + C_z \cdot E_{q3} + \delta. \tag{41}$$

(2) Compensation channel cross-coupling gain

After the contour error, ϵ , is calculated using the cross-coupling controller, the contour error compensation amount, ϵ_c , is obtained. It is converted into the task space of the parallel module, and the contour error, ϵ_r , is obtained in the fixed platform coordinate system using Eq. (33) as follows:

$$\epsilon_r = [\epsilon_{rx} \quad \epsilon_{ry} \quad \epsilon_{rz}]^T = \begin{bmatrix} t & n & b \end{bmatrix}_{3 \times 3} \cdot \epsilon_c, \tag{42}$$

Thus, the position loop compensations, u_{q1} , u_{q2} , and u_{q3} , of the three driving branches in the joint space corresponding to the task space compensation are as follows:

$$u_q = J_e \epsilon_r, \tag{43}$$

where $u_q = [u_{q1} \quad u_{q2} \quad u_{q3}]^T$.

Combining Fig. 7 and Eqs. (42) and (43), the gain coefficient matrix of the compensation channel is obtained as follows:

$$\begin{cases} C_{q1} = J_e(1, :) \cdot \begin{bmatrix} t & n & b \end{bmatrix}_{3 \times 3} \\ C_{q2} = J_e(2, :) \cdot \begin{bmatrix} t & n & b \end{bmatrix}_{3 \times 3} \\ C_{q3} = J_e(3, :) \cdot \begin{bmatrix} t & n & b \end{bmatrix}_{3 \times 3} \end{cases}, \tag{44}$$

(3) Lyapunov stability analysis

According to Eq. (28), the observer of linear system can be defined as:

$$\begin{cases} \dot{\hat{x}} = A\hat{x} + Bu + O_g(y - \hat{y}) \\ \hat{y} = C^T \hat{x} \end{cases} \tag{45}$$

where O_g is the observation gain matrix. Then the dynamic error can be expressed as:

$$E = (A - O_g C^T) \tilde{x} \tag{46}$$

where \tilde{x} is the state estimation error matrix. From Fig. 7, the tracking error $\tilde{x} = [E_{q1}, E_{q2}, E_{q3}]$ of the single-axis UPS branch chain of the control system can be expressed as:

$$E_{q1} = l_1 \frac{(1 - G_1^P)(1 + C_{q1} C_x G_c G_1^P)}{1 + C_l G_c} + l_2 \frac{(1 - G_2^P) C_{q1} C_y G_c G_1^P}{1 + C_l G_c} + l_3 \frac{(1 - G_3^P) C_{q1} C_z G_c G_1^P}{1 + C_l G_c} + \frac{G_c C_{q1} \delta G_1^P}{1 + C_l G_c} \tag{47}$$

$$E_{q2} = l_1 \frac{(1 - G_1^P) C_{q2} C_x G_c G_2^P}{1 + C_l G_c} + l_2 \frac{(1 - G_2^P)(1 + C_{q2} C_y G_c G_2^P)}{1 + C_l G_c} + l_3 \frac{(1 - G_3^P) C_{q2} C_z G_c G_2^P}{1 + C_l G_c} + \frac{G_c C_{q2} \delta G_2^P}{1 + C_l G_c} \tag{48}$$

$$E_{q_3} = l_1 \frac{(1 - G_1^P) C_{q_3} C_x G_c G_3^P}{1 + C_l G_c} + l_2 \frac{(1 - G_2^P) C_{q_3} C_y G_c G_3^P}{1 + C_l G_c} + l_3 \frac{(1 - G_3^P) (1 + C_{q_3} C_z G_c G_3^P)}{1 + C_l G_c} + \frac{G_c C_{q_3} \delta G_3^P}{1 + C_l G_c} \tag{49}$$

where $C_l = G^p_1 C_{q_1} C_x + G^p_2 C_{q_2} C_y + G^p_3 C_{q_3} C_z$.

Similarly, from Fig. 7, the system input $x = [q_1, q_2, q_3]$ adjusted by the multi-axis cross-coupling contour control system is deduced, and the following is obtained:

$$q_1 = l_1 \frac{1 + (C_{q_1} C_x + C_{q_1} C_x G_1^P) G_c}{1 + C_l G_c} + l_2 \frac{C_{q_1} C_y (1 + G_2^P) G_c}{1 + C_l G_c} + l_3 \frac{C_{q_1} C_z (1 + G_3^P) G_c}{1 + C_l G_c} + \frac{G_c C_{q_1} \delta}{1 + C_l G_c} \tag{50}$$

$$q_2 = l_1 \frac{C_{q_2} C_x (1 + G_1^P) G_c}{1 + C_l G_c} + l_2 \frac{1 + (C_{q_2} C_y + C_{q_2} C_y G_2^P) G_c}{1 + C_l G_c} + l_3 \frac{C_{q_2} C_z (1 + G_3^P) G_c}{1 + C_l G_c} + \frac{G_c C_{q_2} \delta}{1 + C_l G_c} \tag{51}$$

$$q_3 = l_1 \frac{C_{q_3} C_x (1 + G_1^P) G_c}{1 + C_l G_c} + l_2 \frac{C_{q_3} C_y (1 + G_2^P) G_c}{1 + C_l G_c} + l_3 \frac{1 + (C_{q_3} C_z + C_{q_3} C_z G_3^P) G_c}{1 + C_l G_c} + \frac{G_c C_{q_3} \delta}{1 + C_l G_c} \tag{52}$$

Based on Eqs. (50)–(52), system inputs $q_1, q_2,$ and q_3 regulated by the cross-coupling controller are cross-coupling terms. The cross-coupling control system outputs a certain correction signal based on the contour error generated by the OMPR during the contour movement process and compensates it to the position loop input end of the single-joint control system, completing the closed-loop contour control.

Based on this, the Lyapunov closed-loop equation can be constructed as follows:

$$V(t) = x^T P x + \frac{1}{2} E^T P_1 E \tag{53}$$

where $P = P^T > 0$ and $P_1 = P_1^T > 0$.

The necessary and sufficient conditions for the stability of the control system are as follows: for the scalar function V with continuous first-order partial derivative, if V is positive definite and \dot{V} is negative definite. Given $Q = Q^T > 0, Q_0 = Q_0^T > 0,$ and

$$\begin{cases} -Q = -PA - A^T P \\ -Q_1 = (A - O_g C^T)^T P_1 + P_1 (A - O_g C^T) \end{cases} \tag{54}$$

Find the full derivative of $V,$

$$\dot{V} = -x^T Q x - E^T Q_1 E. \tag{55}$$

Order, $Q_0 = \begin{bmatrix} Q & 0 \\ 0 & \frac{1}{2} Q_1 \end{bmatrix}$. Then,

$$\dot{V} = \begin{bmatrix} x^T & E^T \end{bmatrix} Q_0 \begin{bmatrix} x \\ E \end{bmatrix} \leq -\lambda_{\min}(Q_0) \left\| \begin{bmatrix} x \\ E \end{bmatrix} \right\|^2 \tag{56}$$

where $\lambda_{\min}(Q_0)$ is the minimum eigenvalue of matrix Q_0 . Because of $\lambda_{\min}(Q_0) > 0,$ it can prove that \dot{V} is negative definite, and it is proved that the closed-loop system is asymptotically stable.

(4) Simulation analysis

According to the feedforward combined multi-axis cross-coupling contour control system established, the control system is simulated and analyzed by Matlab/Simulink. Three trajectories of line, arc, and spiral in the world coordinate system are analyzed respectively. The trajectory equations are

$$\begin{aligned}
 \text{Line: } & \begin{cases} X = 70t - R_g \\ Y = 0 \times t_1 & t_1 = 0: 10 \\ Z = 0 \times t_1 + 1097 \end{cases} \\
 \text{Arc: } & \begin{cases} X = 200 \cos \left(0.2\pi t_2 + \frac{3}{2}\pi \right) \\ Y = 200 \sin \left(0.2\pi t_2 + \frac{3}{2}\pi \right) & t_2 = 0: 10 \\ Z = 0 \times t_2 + 1097 \end{cases} \tag{57} \\
 \text{Spiral: } & \begin{cases} X = 20t_3 \cos \left(\frac{\pi}{2}t_3 + \frac{\pi}{2} \right) \\ Y = 20t_3 \sin \left(\frac{\pi}{2}t_3 + \frac{\pi}{2} \right) & t_3 = 0: 10 \\ Z = 0 \times t_3 + 1097 \end{cases}
 \end{aligned}$$

As can be seen from Fig. 9(a), when only cross-coupling contour control is used for compensation, the contour error is significantly reduced. When the feedforward combined multi-axis cross-coupling contour control is used, the contour error is reduced from 0.015 to 0.004 mm, and the overall variation law of contour error is smoother. It can be seen from Fig. 9(b) that the contour error of the arc trajectory presents a regular fluctuating trend, which is caused by the error accumulation of the motion branch. When the feedforward combined multi-axis cross-coupling contour control is used, the error is reduced from the peak value of 0.193 to 0.018 mm. As can be seen from Fig. 9(c), with the increase of spiral contour, the contour error also increases, and the maximum contour error is obtained at the maximum curvature. Using feedforward combined multi-axis cross-coupling contour control, the maximum contour error can be reduced from 0.218 to 0.022 mm, and the variation trend of contour error is smoother. Therefore, the designed feedforward combined multi-axis cross-coupling contour control can effectively reduce the contour error, and the effect is better than the cross-coupling contour compensation control.

5. Experimental analysis

To verify the effectiveness of the established contour control model, a control system is built for the OMPR. Contour control experiments are conducted for three types of common trajectories in optical mirror processing. The experimental site and the topology of CCOS are shown in Fig. 10. The multi-axis motion controller is a programmable multi-axes controller (PMAC). On a PC, the path contour of the grinding tool in the world coordinate system is planned. Considering that the numerical search method for the inverse solution of the series module reduces the operation speed of the controller, the PC is used for the offline inverse solution of the series module. Moreover, the angle change of the two series swivel heads and the position of the parallel module moving platform are input to the PMAC to complete the control task. The displacement and velocity of five axes of the machining robot are collected, and the position and velocity of the end execution point are calculated through the forward kinematics model.

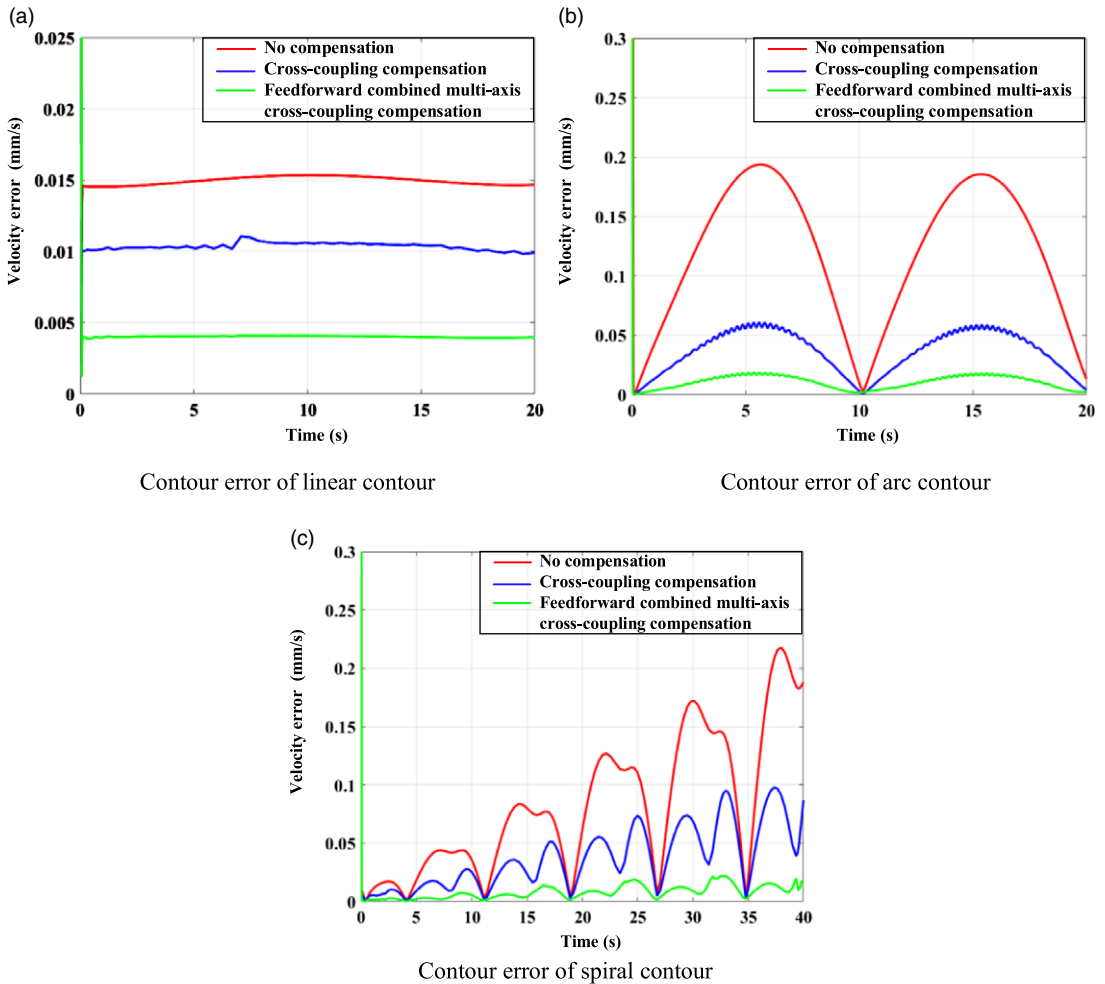


Figure 9. Contour error simulation.

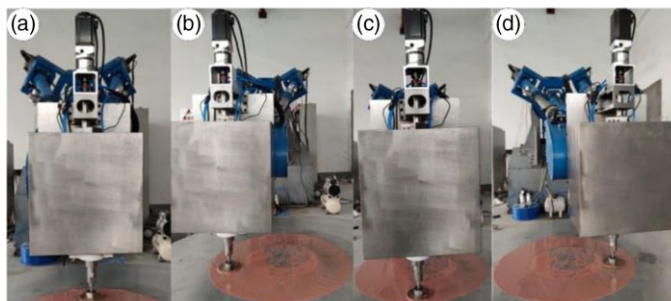


Figure 10. Experimental site.

Because the CCOS has pneumatic active position compensation function in the Z axis direction, only the motion parameters in the X and Y directions have research significance. During the experiment, the revolution speed of CCOS grinding system was set to 30 r/min and the rotation speed was set to 180 r/min. The linear contour, arc contour, and spiral contour are tested respectively. The trajectory equation is the same as the simulation trajectory, as shown in Eq. (57).

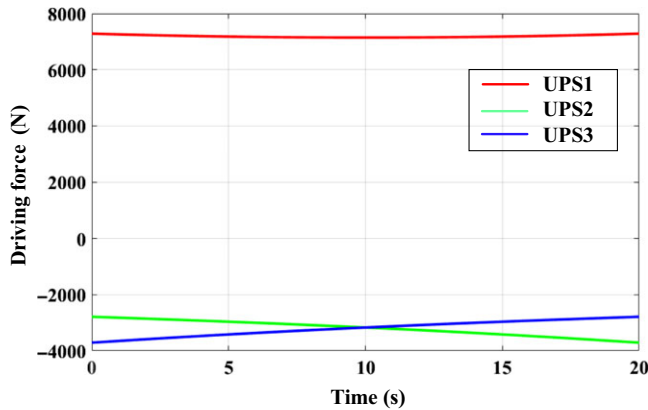


Figure 11. Driving force output signal in linear contour linear contour.

5.1 Linear contour control compensation experiment

In the experiment, the trajectory of the grinding tool was a linear contour along the X axis of the world coordinate system, the length is 700 mm, the movement period was 20 s, and the sampling period was 20 ms. The experiment was conducted on an aluminum plate instead of an optical mirror. Based on the established contour error model, the contour error of the OMPR can be obtained by mapping the tracking error of each joint of the parallel module to the workspace. During the experiment, no compensation control, traditional cross-coupling compensation, and feedforward combined multi-axis cross-coupling compensation contour control experiments were conducted. The torque control mode is adopted for the linear contour experiment, and the driving force of the three driving branches in the experiment of feedforward combined multi-axis cross-coupling contour control compensation is shown in Fig. 11. Due to the inclined arrangement of the OMPR, the gravity is different in the three driving components. In order to counteract gravity, the UPS1 needs to output the force pointing to the moving platform along the branch chain, which is specified as the positive direction here. The UPS2 and UPS3 need to output the force pointing to the fixed platform along the branch chain, which is specified as the negative direction here. The UPS1 bears most of the gravity component, so the output force of the UPS1 is the largest.

The experimental results are shown in Fig. 12. When using the traditional PID control, the contour error generated by the parallel modules is approximately 0.027 mm. When using the traditional cross-coupling compensation control strategy, the contour error is reduced to 0.018 mm. When the feedforward combined multi-axis cross-coupling control strategy is used for compensation, the contour error is further reduced to 0.006 mm. The variation trend of the experimental value and the theoretical value is the same, and the difference is only 0.002 mm, which is caused by the random error of the robot. It can be seen that the effect of the feedforward combined multi-axis cross-coupling control strategy is better than that of the traditional multi-axis cross-coupling control system.

The velocity stability has a direct impact on the surface accuracy of the optical mirror. In the experiment, the velocity errors in X and Y directions in the processing of the optical mirror were tested respectively. The experimental results are shown in Fig. 13. When the compensation control mode is not adopted, the velocity errors in the X and Y directions of the linear contour are 0.025 and 0.021 mm/s. Through traditional cross-coupling compensation, the velocity errors in X and Y directions are reduced to 0.013 and 0.019 mm/s. Through feedforward combined multi-axis cross-coupling contour control, the velocity errors in X and Y directions are reduced to 0.005 and 0.006 mm/s. Therefore, the designed control compensation strategy not only reduces the velocity errors of the OMPR but also makes its motion more stable.

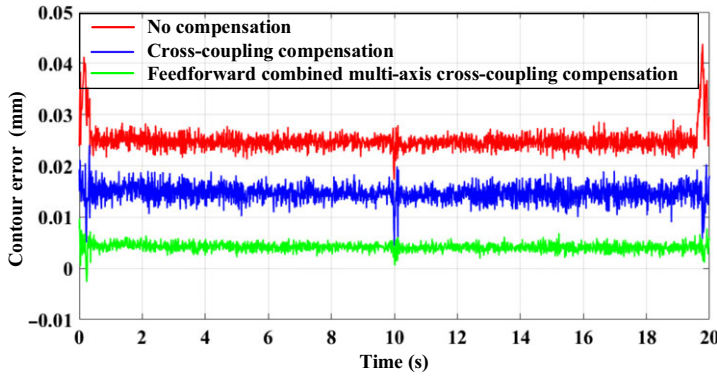


Figure 12. Experiment of linear contour error control compensation.

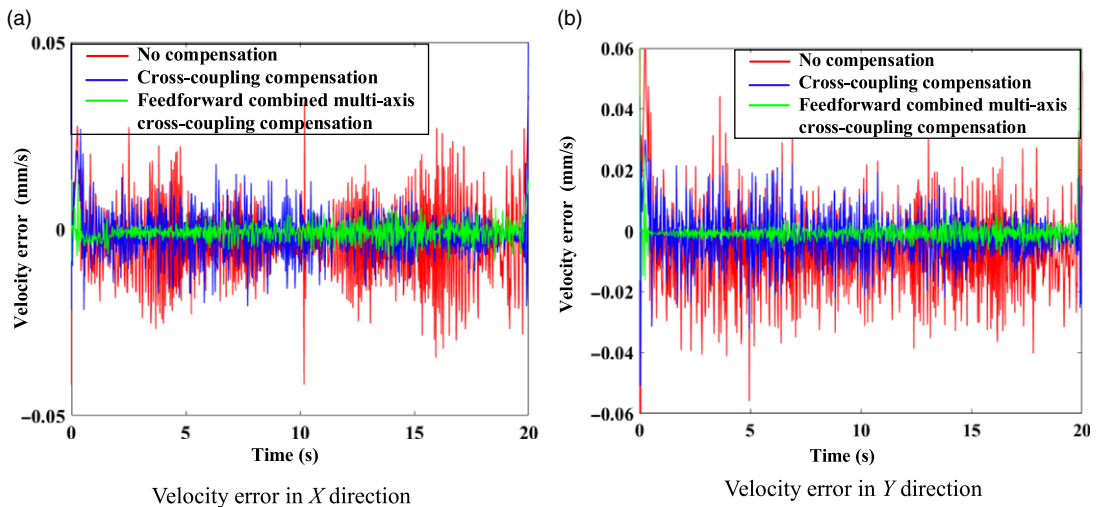


Figure 13. Linear contour velocity error.

5.2 Arc contour control compensation experiment

Taking the machined mirror as the center point, given the space arc contour trajectory of the grinding tool radius of 200 mm, the movement period is 20 s, and the sampling period is 20 ms. The experimental steps are the same as those of the linear contour control experiment. The torque control mode is adopted for the arc contour experiment, and the driving force of the three driving branches in the experiment of feedforward combined multi-axis cross-coupling contour control compensation is shown in Fig. 14. During the movement along the arc contour, the three UPS branch chains have the process of elongation and shortening. When the branch chain moves to the longest position, the heavy torque is the largest, and the driving force output value also reaches the maximum.

The experimental results are shown in Fig. 15. When the control compensation is not conducted, the contour error of the OMPR is approximately sinusoidal, and the error peak is 0.223 mm. When the traditional cross-coupling compensation control strategy is adopted, the contour error is reduced to 0.069 mm. When the feedforward combined multi-axis cross-coupling control strategy is used for compensation, the contour error is further reduced to approximately 0.021 mm. The variation trend of the experimental value and the theoretical value is the same, and the difference is only 0.003 mm. It is verified that the feedforward combined multi-axis cross-coupling control strategy still exhibits good compensation performance in a circular motion trajectory.

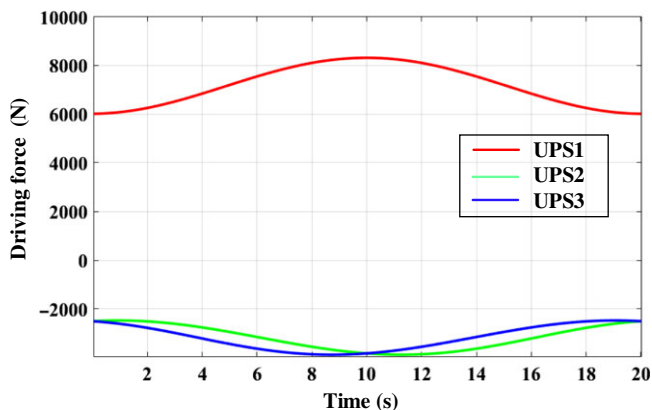


Figure 14. Driving force output signal in linear contour arc contour.

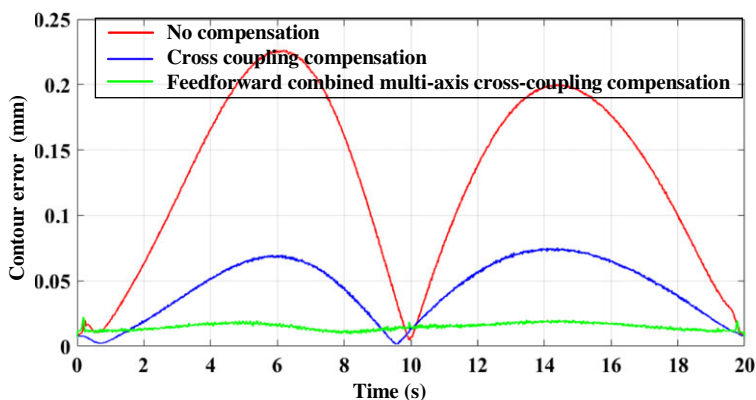


Figure 15. Experiment of arc contour error control compensation.

At the same time, the velocity errors in X and Y directions during processing of the optical mirror under arc contour are collected. The experimental results are shown in Fig. 16. When the compensation control mode is not adopted, the velocity errors in the X and Y directions of the arc contour are 0.055 and 0.051 mm/s. Through traditional cross-coupling compensation, the velocity errors in X and Y directions are reduced to 0.031 and 0.028 mm/s. Through feedforward combined multi-axis cross-coupling contour control, the velocity errors in X and Y directions are reduced to 0.008 and 0.010 mm/s. It can be seen that the designed control strategy also has a good effect on the velocity error compensation of arc contour.

5.3 Spiral contour control compensation experiment

The given end grinding tool is a spiral contour with the starting point at the origin of the world coordinate system, the movement time is 40 s, and the sampling period is 40 ms. The experimental steps are the same as before. The torque control mode is adopted for the spiral contour experiment, and the driving force of the three driving branches in the experiment of feedforward combined multi-axis cross-coupling contour control compensation is shown in Fig. 17. When the OMPR moves along the spiral contour, the amplitude of elongation and shortening of the three UPS branches increases with the gradual increase of the curvature radius of the spiral.

The experimental results are shown in Fig. 18. For the spiral contour, the contour error at the end of the parallel module in the control system increases as the curvature of the spiral increases. When using the traditional PID control, the maximum contour error is 0.213 mm. When the traditional cross-coupling

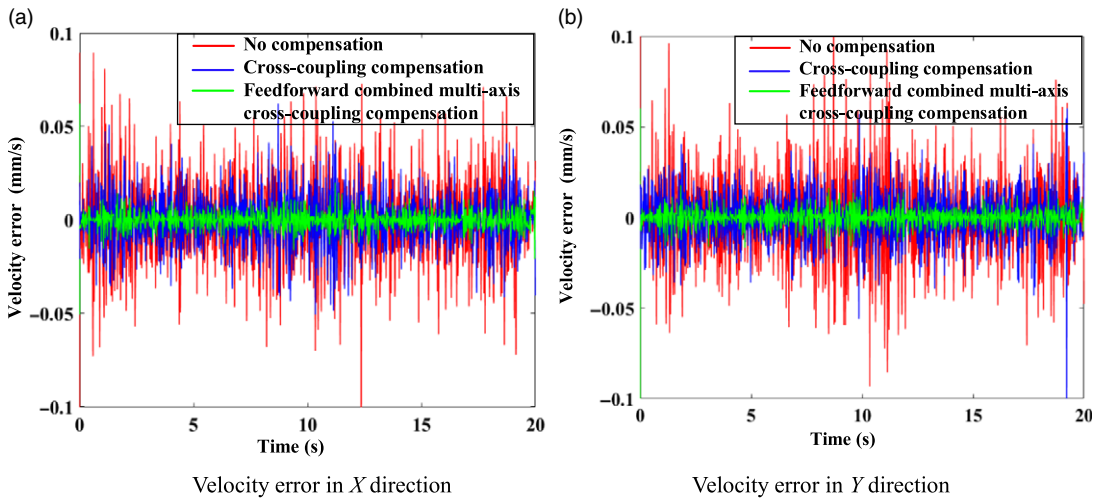


Figure 16. Arc contour velocity error.

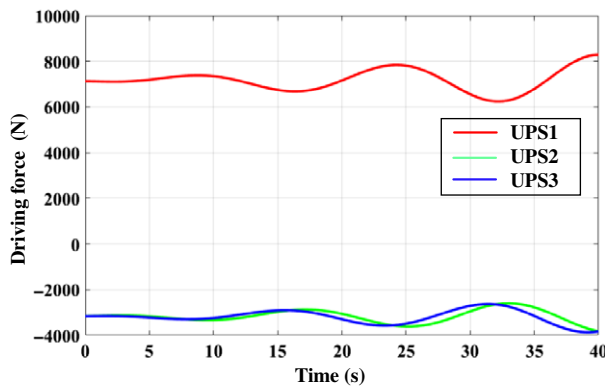


Figure 17. Driving force output signal in linear contour spiral contour.

compensation control strategy is adopted, the contour error is reduced to approximately 0.121 mm. When the feedforward combined multi-axis cross-coupling control strategy is used for compensation, the contour error is further reduced to approximately 0.030 mm. The variation trend of the experimental value and the theoretical value is the same, and the difference is only 0.008 mm. It can be seen that the feedforward combined multi-axis cross-coupling control strategy also exhibits good compensation performance in the spiral trajectory.

Similarly, the velocity errors of the OMPR in the X and Y directions under the spiral contour are measured. The experimental results are shown in Fig. 19. With the increase of the curvature of the spiral contour, the motion velocity errors of the machining robot in the X and Y directions also fluctuate greatly with the increase of the curvature. When the compensation control mode is not adopted, the velocity errors in the X and Y directions of the arc contour are 0.083 and 0.062 mm/s. Through traditional cross-coupling compensation, the velocity errors in X and Y directions are reduced to 0.037 and 0.025 mm/s. Through feedforward combined multi-axis cross-coupling contour control, the velocity errors in X and Y directions are reduced to 0.011 and 0.010 mm/s. It can be seen that the designed control strategy also has a good effect on the trajectory of large curvature.

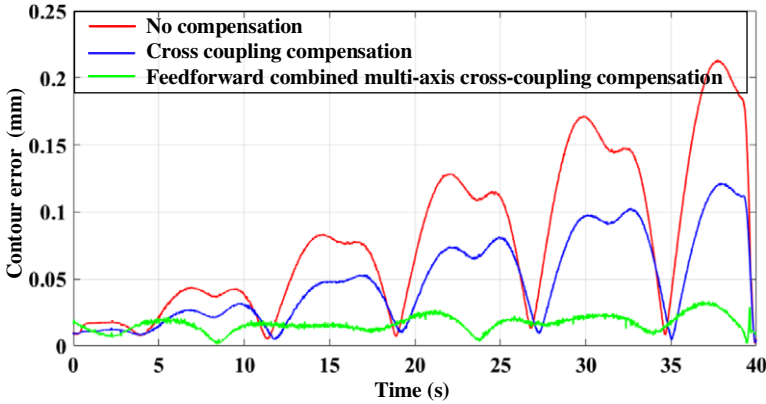


Figure 18. Experiment of spiral contour error control compensation.

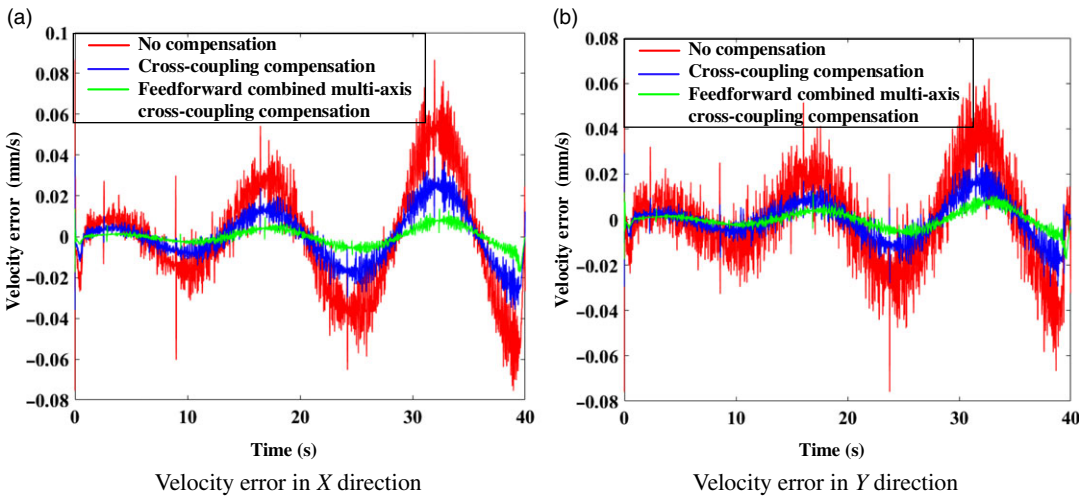


Figure 19. Spiral contour velocity error.

6. Conclusion

This study is aimed at the problem of the contour error generated during the processing of an OMPR, which decreases the accuracy of an optical mirror surface. Considering an OMPR under specific task trajectories of the optical mirror technology, its contour error and control compensation strategy are researched and analyzed. Considering that the world coordinate system is convenient for describing the contour error of an optical mirror in the process of optical mirror machining, the robot workspace is transformed into the world coordinate system to analyze the machining trajectory. Based on the principle of differential geometry, the Frenet coordinate system is established. Using the tangential approximation and osculating circle approximation methods, three-dimensional contour error models of the OMPR in grid trajectory, concentric circle trajectory, and spiral trajectory processing modes are derived. The control strategy of the entire machine is determined, and a parallel module feedforward combined multi-axis cross-coupling control system is built. Based on the kinematic transformation relationship, the contour error control, feedforward channel gain, and compensation channel gain models are established in the parallel module task space. Subsequently, the transfer function of the cross-coupling system is obtained, and the key control variables and stability of the system are analyzed to ensure the theoretical stability of the control system. Finally, an experimental analysis is conducted on an experimental prototype, and the

results show that the established feedforward combined multi-axis cross-coupling control compensation strategy can achieve a good compensation effect on the straight line, arc, and spiral machining trajectories of the optical mirror. The contour errors were reduced to 22.2%, 9.4%, and 14.1%, respectively. Moreover, through the feedforward combined multi-axis cross-coupling control compensation strategy, the speed error of the OMPR is also greatly reduced. The speed error in the X and Y directions of the linear contour is reduced to 20.0% and 28.6%, respectively; the speed error in the X and Y directions of the arc contour is reduced to 14.5% and 19.6%, respectively; and the speed error in the X and Y directions of the spiral contour is reduced to 13.3% and 16.1%, respectively.

The feedforward combined multi-axis cross-coupling control compensation strategy can effectively reduce the contour error of the OMPR. It provides a theoretical basis for a robot to directly face the precision processing object using the control and compensation strategy in a future research study to improve the molding accuracy of a surface and optimize the processing technology of a large-scale optical mirror. It also provides an experimental basis for improving the surface forming accuracy, reducing the number of iterations, and optimizing the processing technology of large-scale optical mirrors in the future using control and compensation strategies. Simultaneously, it provides a feasible case for the application of a five-DOF hybrid robot in the processing of ultra-precision machining.

Acknowledgement. The financial support for this study provided by the Priority Academic Program Development of Jiangsu Higher Education Institutions and the National Natural Science Foundation of China (Grant No. 91648105) is gratefully acknowledged.

Declaration of conflicting interests. The authors declared no potential conflicts of interest with respect to the research, authorship, and/or publication of this article.

References

- [1] Z. Jin, G. Cheng, S. Chen and F. Guo, "Human-machine-environment information fusion and control compensation strategy for large optical mirror processing system," *Proc. Inst. Mech. Eng. Part C-J. Eng. Mech. Eng. Sci.* **0954406220959689** (2020).
- [2] C. Jiao, Y. Shu, Y. Chen and Z. Zhang, "The kinematics solving algorithm of single-axis polishing machine," *Optik* **224**, 165436 (2020).
- [3] B. Jiang, D. Zhao, B. Wang, H. Zhao, Y. Liu and X. Lu, "Flatness maintenance and roughness reduction of silicon mirror in chemical mechanical polishing process," *Sci. China-Technol. Sci.* **63**(1), 166–172 (2020).
- [4] Y. Kong, G. Cheng, F. Guo, W. Gu and L. Zhang, "Inertia matching analysis of a 5-DOF hybrid optical machining manipulator," *J. Mech. Sci. Technol.* **33**(10), 4991–5002 (2019).
- [5] M. Hosseini and H. Daniali, "Cartesian workspace optimization of Tricept parallel manipulator with machining application," *Robotica* **33**(9), 1948–1957 (2012).
- [6] S. Farooq, A. Baqai and M. Shah, "Optimal design of tricept parallel manipulator with particle swarm optimization using performance parameters," *J. Eng. Res.* **9**(2), 378–395 (2021).
- [7] J. Li, F. Ye, N. Shen, Z. Wang and L. Geng, "Dimensional synthesis of a 5-DOF hybrid robot," *Mech Mach. Theory* **150**, 103865 (2020).
- [8] A. Gutierrez-Giles and M. Arteaga-Perez, "Output feedback hybrid force/motion control for robotic manipulators interacting with unknown rigid surfaces," *Robotica* **38**(1), 136–158 (2020).
- [9] S. Hu, "Motion error analysis for a 3-dof parallel robot," *Adv. Mater. Res.-SWITZ* **460**, 347–350 (2012).
- [10] S. Ibaraki and M. Hiruya, "Assessment of non-rigid body, direction-and-velocity-dependent error motions and their cross-talk by two-dimensional digital scale measurements at multiple positions," *Precis Eng.-J. Int. Soc. Precis. Eng. Nanotechnol.* **66**(2), 144–153 (2020).
- [11] X. Li, X. Li, Q. Cheng, R. Li, W. Deng, X. Luo, F. Zhang, D. Xue and X. Zhang, "Optimized strategy to restrain the mid-spatial-frequency surface error in computer-controlled optical surfacing," *Results Phys.* **19**(C), 103356 (2020).
- [12] H. Zhang, L. Li, J. Zhao, J. Zhao, S. Liu and J. Wu, "Design and implementation of hybrid force/position control for robot automation grinding aviation blade based on fuzzy PID," *Int. J. Adv. Manuf. Technol.* **107**(3–4), 1741–1754 (2020).
- [13] X. Yang, R. Seethaler, C. Zhan, D. Lu and W. Zhao, "A model predictive contouring error precompensation method," *IEEE Trans. Ind. Electron.* **67**(5), 4036–4045 (2020).
- [14] B. Liu, M. Xu, J. Fang and Y. Shi, "A feedrate optimization method for CNC machining based on chord error reevaluation and contour error reduction," *Int. J. Adv. Manuf. Technol.* **111**(11–12), 3437–3452 (2020).
- [15] A. Izadbakhsh, S. Khorashadizadeh and P. Kheirkhahan, "Tracking control of electrically driven robots using a model-free observer," *Robotica* **37**(4), 729–755 (2019).

- [16] X. Du, J. Huang, L. Zhu and H. Ding, "Sliding mode control with third-order contour error estimation for free-form contour following," *Precis. Eng.-J. Int. Soc. Precis. Eng. Nanotechnol.* **66**, 282–294 (2020).
- [17] M. Yang, J. Yang, L. Zhu and X. Yu, "A novel curvature circle iterative algorithm for contour error control of multi-axis CNC machine tools," *Precis. Eng.-J. Int. Soc. Precis. Eng. Nanotechnol.* **65**, 23–31 (2020).
- [18] D. Song, J. Ma, Y. Zhong and J. Yao, "Definition and estimation of joint-space contour error based on generalized curve for five-axis contour following control," *Precis. Eng.-J. Int. Soc. Precis. Eng. Nanotechnol.* **65**(1–4), 32–43 (2020).
- [19] J. Ma, G. Li, X. Lu, Z. Jia, F. Qin and Z. Qu, "Toolpath regeneration in subregional contour-parallel processing based on isoscallop method," *IEEE-ASME Trans. Mechatron.* **26**(2), 730–740 (2021).
- [20] Q. Hu, Y. Chen and J. Yang, "On-line contour error estimation and control for corner smoothed five-axis tool paths," *Int. J. Mech. Sci.* **171**(6), 105377 (2020).
- [21] Z. Wang, C. Hu and Y. Zhu, "Double Taylor expansion-based real-time contouring error estimation for multiaxis motion systems," *IEEE Trans. Ind. Electron.* **66**(12), 9490–9499 (2019).
- [22] D. Song, Y. Zhong and J. Ma, "Third-order contour-error estimation for arbitrary free-form paths in contour-following tasks," *Precis. Eng.-J. Int. Soc. Precis. Eng. Nanotechnol.* **60**(1–4), 85–92 (2019).
- [23] X. Sheng and L. Wang, "A comparison strategy for improving the precision of contour error estimation," *Int. J. Precis. Eng. Manuf.* **20**(8), 1395–1403 (2019).
- [24] X. Yang, R. Seethaler, C. Zhan, D. Lu and W. Zhao, "A novel contouring error estimation method for contouring control," *IEEE-ASME Trans. Mechatron.* **24**(4), 1902–1907 (2019).
- [25] C. Hu, Z. Wang, Y. Zhu and M. Zhang, "Accurate three-dimensional contouring error estimation and compensation scheme with zero-phase filter," *Int. J. Mach. Tools Manuf.* **128**(11), 33–40 (2018).
- [26] T. Zhang, C. Wu and Y. Zou, "Chord error constraint based integrated control strategy for contour error compensation," *Front. Mech. Eng.* **15**(4), 645–658 (2020).
- [27] A. Izadbakhsh, S. Khorashadizadeh and S. Ghandali, "Robust adaptive impedance control of robot manipulators using Szasz-Mirakyan operator as universal approximator," *ISA Trans.* **106**(5), 1–11 (2020).
- [28] Y. Wang, W. Zhang, H. Dong and L. Yu, "A LADRC based fuzzy PID approach to contour error control of networked motion control system with time-varying delays," *Asian J. Control* **22**(5), 1973–1985 (2020).
- [29] K. Li, S. Boonto and T. Nuchkrua, "On-line self tuning of contouring control for high accuracy robot manipulators under various operations," *Int. J. Control Autom. Syst.* **18**(7), 1818–1828 (2020).
- [30] M. Chen, Y. Sun and J. Xu, "A new analytical path-reshaping model and solution algorithm for contour error pre-compensation in multi-axis computer numerical control machining," *J. Manuf. Sci. Eng.-Trans. ASME* **142**(6), 061006 (2020).
- [31] J. Li, Y. Wang, Y. Li and W. Luo, "Reference trajectory modification based on spatial iterative learning for contour control of two-axis NC systems," *IEEE-ASME Trans. Mechatron.* **25**(3), 1266–1275 (2020).
- [32] Z. Wang, C. Hu and Y. Zhu, "Dynamical model based contouring error position-loop feedforward control for multiaxis motion systems," *IEEE Trans. Ind. Inform.* **15**(8), 4686–4695 (2019).
- [33] T. Duong, P. Rodriguez-Ayerbe, S. Lavernhe, C. Tournier and D. Dumur, "Contour error pre-compensation for five-axis high speed machining: offline gain adjustment approach," *Int. J. Adv. Manuf. Technol.* **100**(9–12), 3113–3125 (2019).
- [34] C. Cho, Y. Song, C. Lee and H. Kim, "Neural network-based real time PID gain update algorithm for contour error reduction," *Int. J. Precis. Eng. Manuf.* **19**(11), 1619–1625 (2018).
- [35] Y. Liu, L. Liang, T. Chu and M. Wu, "N-PD cross-coupling synchronization control based on adjacent coupling error analysis," *J. Cent. South Univ.* **25**(5), 1154–1164 (2018).
- [36] Z. Wang, C. Hu, Y. Zhu, S. He, M. Zhang and H. Mu, "Newton-ILC contouring error estimation and coordinated motion control for precision multiaxis systems with comparative experiments," *IEEE Trans. Ind. Electron.* **65**(2), 1470–1480 (2018).
- [37] P. Ouyang, T. Dam and V. Pano, "Cross-coupled PID control in position domain for contour tracking," *Robotica* **33**(6), 1351–1374 (2015).